Analyst

PAPER

View Article Online
View Journal | View Issue

Cite this: *Analyst*, 2022, **147**, 1567

Sizing individual dielectric nanoparticles with quantitative differential interference contrast microscopy†

Samuel Hamilton, [a] David Regan, [a] Lukas Payne, [a,b] Wolfgang Langbein *[b] and Paola Borri [a]

We report a method to measure the size of single dielectric nanoparticles with high accuracy and precision using quantitative differential interference contrast (DIC) microscopy. Dielectric nanoparticles are detected optically by the conversion of the optical phase change into an intensity change using DIC. Phase images of individual nanoparticles were retrieved from DIC by Wiener filtering, and a quantitative methodology to extract nanoparticle sizes was developed. Using polystyrene beads of 100 nm radius as size standard, we show that the method determines this radius within a few nm accuracy. The smallest detectable polystyrene bead is limited by background and shot-noise, which depend on acquisition and analysis parameters, including the objective numerical aperture, the DIC phase offset, and the refractive index contrast between particles and their surrounding. Measurements on small beads of 15 nm nominal radius are shown, and a sensitivity limit potentially reaching down to 1.8 nm radius was inferred. As application example, individual nanodiamonds with nominal sizes below 50 nm were measured, and were found to have a nearly exponential size distribution with 28 nm mean value. Considering the importance of dielectric nanoparticles in many fields, from naturally occurring virions to polluting nanoplastics, the proposed method could offer a powerful quantitative tool for nanoparticle analysis, combining accuracy, sensitivity and high-throughput with widely available and easy-to-use DIC microscopy.

Received 5th November 2021,
Accepted 14th February 2022

DOI: 10.1039/d1an02009a

rsc.li/analyst

1. Introduction

Dielectric nanoparticles (NPs) exist in a multitude of forms and are ubiquitous in our world. They can be naturally occurring (*e.g.* virions and exosomes), synthetically fabricated (*e.g.* silica beads, nanodiamonds), or by-products of material degradation (*e.g.* nanoplastics). These NPs are widely utilised in research and industry, with applications ranging from drug delivery in biomedicine[1,2] to the fabrication of advanced functional materials.[3] A key requirement for all these applications is the knowledge of the NP size. For example, in cell biology it is well known that the uptake of a NP by the plasma membrane, and the subsequent intracellular trafficking route, tightly depends on the NP size, which in turn is acrucial parameter in the use of NPs as vehicles for drug delivery and therapeutics.[1,2]

Different from metallic particles, dielectric NPs are typically not electron dense, hence their sizes are more challenging to measure with electron microscopy (EM), the industry-standard technique for NP characterisation. EM analysis is also expensive and typically "low-throughput", since only a limited number of NPs can be examined in one field of view under vacuum (for a review on NP characterisation methods see ref. 4 and 5). To that end, the use of wide-field optical microscopy to determine the size of individual NPs offers many advantages, including simplicity, low cost, high speed and high throughput, with hundreds of individual NPs rapidly imaged in one field of view, under ambient conditions. However, the spatial resolution of an optical microscope is limited by light diffraction (usually to about 200 nm), typically larger than the size of the investigated NPs. In other words, differently from EM, optical microscopy methods cannot directly resolve NP dimensions. On the other hand, they can exploit the physical relationship between measurable optical properties and NP sizes to accurately determine the latter. Using this concept, we recently showed that NP sizes could be determined from the optical absorption (σ_{abs}) and scattering cross-section (σ_{sca}) of individual NPs measured by wide-field extinction microscopy, with uncertainties down to about 1 nm in diameter.[6]

[a]*School of Biosciences, Cardiff University, Cardiff, UK*
[b]*School of Physics and Astronomy, Cardiff University, Cardiff, UK.*
E-mail: langbeinww@cardiff.ac.uk

†Electronic supplementary information (ESI) available. See DOI: 10.1039/d1an02009a

While optical extinction microscopy is in principle applicable to any NP material, for particle sizes much smaller than the light wavelength (dipole limit) the technique is practically useful only when NPs exhibit significant optical absorption, such as gold[6] and silver NPs.[7] This is because σ_{abs} scales with the NP volume while σ_{sca} scales with the square of the NP volume, severely penalising small NPs which are not absorptive. In other words, by measuring the magnitude of $\sigma_{ext} = \sigma_{abs} + \sigma_{sca}$ one can be sensitive to small NP sizes only if particles are strongly absorbing such that $\sigma_{ext} \sim \sigma_{abs}$. For example, using gold NPs, we have demonstrated a sensitivity limit down to sizes of 2 nm diameter.[8] For significantly larger diameters, quantitative extinction and scattering measurements can be used, together with simulations, to extract sizes of dielectric NPs, as shown for 100 nm polystyrene (PS) beads in ref. 9.

We note that light scattering can also be exploited to determine the hydrodynamic radius of NPs diffusing in a liquid of known viscosity.[14] Commercial instruments are available, either as ensemble measurements techniques (using dynamic light scattering) or by tracking individual particles (nanoparticle tracking analysis). In addition to the mentioned limitation of light scattering methods penalizing small NPs, these techniques do not measure the geometrical size of a NP. Indeed, the hydrodynamic radius can overestimate the NP geometrical radius, depending *e.g.* on the particle surface charges. Moreover, nanoparticle tracking analysis methods have been shown to overestimate the size distribution.[14]

Small dielectric NPs exhibit a negligible absorption in the visible wavelength range and are weakly scattering. Hence, for such NPs optical sizing by extinction microscopy is less suited and a different optical contrast method is required. Notably, it is possible to achieve an image contrast proportional to the NP volume using interferometric approaches. For example, it has been recently shown that weakly scattering single dielectric nanoparticles (including biological macromolecules) can be detected with high sensitivity by means of reflection microscopy on a weakly reflecting interface, termed interferometric scattering microscopy (iSCAT).[10–12] Alternatively, a transmission technique called COBRI,[13] attenuating the unscattered light similar to conventional phase contrast, has been used to track silica NPs of 50 nm and 100 nm size diffusing in water, with a size sensitivity limit of about 30 nm for these NPs.

One of the simplest interferometric techniques to generate an image contrast scaling with the NP volume exploits the conversion of the optical phase change of transmitted light introduced by the sample into an amplitude change, by means of differential interference contrast microscopy.[15] Briefly, DIC uses a Nomarski prism to split the two linear light polarization components in direction in the condenser back focal plane (BFP), creating a shear distance in the image plane. The two components are recombined by a second prism in the objective BFP. By choosing a shear distance comparable to the spatial resolution of the system, an intensity changing linearly with the differential of the transmitted optical phase along the shear direction is created. Since the phase is proportional to the thickness of an object, the intensity is proportional to the thickness slope. This is akin to the brightness of a modulated surface height under oblique illumination, and thus provides an intuitively interpretable image. DIC also provides optical sectioning since the contrast of a particle decays with the third power of the defocus. Notably, DIC is widely available in most commercial optical microscopes and is commonly used.

To create quantitative phase information from DIC, various methods have been developed in terms of image acquisition and analysis, eventually resulting in a spatially-resolved map of the optical phase, integrated from the differential phase. For example, the acquisition of images for two orthogonal shear directions and four phase offsets, with subsequent Fourier-space phase integration, was simulated by Arnison *et al.*[16] and later experimentally demonstrated by King *et al.*[17] and Duncan *et al.*[18] Alternatively, using only a focussed and a defocussed DIC image, phase retrieval was shown *via* the transport of intensity equation.[19] To simplify the acquisition of two shear directions without sample rotation, two orthogonal Nomarski prisms and polarization control can be employed,[20] and axially-offset circularly-polarized DIC was shown.[21] Moreover, using only a single shear direction, Wiener filtering was demonstrated to be effective in extracting phase images,[22] and iterative phase reconstruction[23] can further improve the results. By exploiting quantitative DIC (qDIC) with Wiener filtering, we have previously shown that the thickness of lipid bilayers could be measured with a precision of 0.1 nm.[24,25] Furthermore, by directly fitting the DIC contrast without phase integration, the lamellarity of giant lipid vesicles was quantified.[26]

The use of qDIC to measure the volume of individual dielectric NPs was proposed by us in an earlier work on single nanodiamonds.[27] However, there the investigated nanoparticles were rather large (200–500 nm diameter) hence the challenge to measure small dielectric NPs with this method was not addressed, neither the detection sensitivity limit, nor the precision or accuracy of the technique was quantified. In this work, we have characterised the application of qDIC for sizing single dielectric NPs and determined the precision and accuracy of the method, depending on the acquisition parameters. As an application example, we show sizing of individual nanodiamonds with only 28 nm mean size.

2. Methods

2.1. Samples

For calibration of the qDIC method, PS beads, having a nominal radius of 100 nm with less than 3% coefficient of variance (cv), were purchased (Alpha Nanotech Colloidal PS Beads NP-PA07CPSX78). These PS beads were dispersed in water and drop cast onto (24 × 24) mm^2 #1.5 coverslips (Menzel Gläser). After drop casting and drying, the beads were immersed in oil by pipetting 20 μl onto the coverslip. To avoid the formation of air bubbles, the samples were then degassed in a vacuum for

10 minutes immediately before adding a microscope slide and sealing the borders using clear nail varnish. Two types of oil were used, namely water immersion oil (Zeiss, Immersol W 2010) of refractive index n_{wo} = 1.334, and silicone oil (Sigma Aldrich, AP 150 Wacker) of index n_{so} = 1.518. Prior to use, all glass slides and coverslips were cleaned as follows. First, coverslips and slides were immersed in toluene and sonicated for 20 minutes, followed by being immersed in acetone and sonicated for 20 minutes. Next, they were immersed in deionized (DI) water which was then boiled for 3 minutes. Finally, slides and coverslips were immersed in a 30% hydrogen peroxide solution, and again sonicated for 20 minutes. After cleaning, slides and coverslips were kept in a refrigerator in the hydrogen peroxide solution, until needed. To demonstrate the sensitivity of the method, fluorescently labelled PS beads of 15 nm nominal radius were purchased (Sigma Aldrich, L5155) and samples were prepared in the same way. Nanodiamonds (NDs) were purchased from Microdiamant with nominal sizes (0–50) nm (MSY 0–0.05 micron), (0–150) nm, (MSY 0–0.15 micron), and (0–250) nm (MSY (0–0.25) micron). Purchased NDs were purified in-house to remove sp^2 graphitic bonds from the surface, by immersion in sulfuric acid for 2 hours, followed by air annealing at 600 °C for 5 hours. Nanodiamonds deposited onto glass were prepared in the same way as described above for PS beads, using silicone oil as surrounding medium.

2.2. Optical setup

DIC images were obtained using an inverted Nikon Ti-U microscope. Samples were illuminated using a 100 W halogen lamp (Nikon V2-A LL 100 W) followed by a Schott BG40 filter to remove wavelengths above 650 nm (for which the DIC polarisers are not suited) and a Nikon green interference filter (Nikon GIF), to define the wavelength range centred at 550 nm and having a full-width at half maximum (FWHM) of 53 nm. Limiting the bandwidth to about 10% of the central wavelength provides a defined average wavelength for the later analysis and limits chromatic errors of the optics. This illumination was then passed through a de-Sénarmont compensator (a rotatable linear polariser and quarter-wave plate, Nikon T-P2 DIC Polariser HT MEN51941) and a Nomarski prism (Nikon N2 DIC module MEH52400 or MEH52500) and focused onto the sample by a condenser of 0.72 numerical aperture (NA) or 1.34 NA (part number MEL56100 or MEL41410, respectively). The shear of the Nikon N2 DIC was measured to be (238 ± 10) nm by removing the condenser DIC module and measuring the image shift for linearly polarized illumination along and across the shear. The objectives used were a 20 × 0.75 NA planapochromat (MRD00205) in conjunction with the 0.72 NA condenser and a 1.5× tube lens, and a 60 × 1.27 NA water immersion planapochromat (MRD70650) or 100 × 1.45 NA oil immersion planapochromat (MRD01905), in conjunction with the 1.34 NA oil immersion condenser and a 1× tube lens. After the objectives, light passes through a suited Nomarski prism (DIC sliders MBH76220, MBH76264, and MBH76190, respectively) and a linear polariser (Nikon Ti-A-E DIC analyser block MEN 51980). Images were detected by a Hamamatsu Orca 285 CCD camera (18 000 electrons full well capacity, 7 electrons read noise, and 4.6 electrons per count, 12 bit digitizer, 1344 × 1024 pixels, pixel size 6.45 μm, 192 counts offset).

The NA of the condenser lens was matched to that of the chosen objective, with the maximum NA of 1.34 used for the 1.45 NA objective, and the maximum of 0.72 for the 0.75 NA objective. The microscope was adjusted for Köhler illumination, and the field aperture was set to be slightly larger than the imaged sample region.

A sequence of N_a frames (up to 256) were acquired, with 120 ms exposure time per frame (given by highest stably achievable frame rate), with the lamp intensity adjusted to provide a mean intensity of about 3000 counts (13 000 photoelectrons) per pixel. Data for de-Sénarmont polarizer angles $\pm\theta$ as well as zero were taken to enable qDIC analysis, for θ of 15, 30, and 45 degrees. Images with opposite angles were taken in close temporal sequence to minimize drift between both data. The rotation of the de-Sénarmont polarizer was motorized (by a home-built modification) to improve positioning speed and reproducibility.

Wide-field *epi*-fluorescence of the labelled PS beads was excited by a metal–halide lamp (Prior Scientific, Lumen L200/D) set at 10% of the maximum power. A suitable exciter/emitter/dichroic filter cube (Semrock, GFP-A-Basic) was used (see also ESI section S3 ii†), resulting in an illumination intensity of about 4 W cm^{-2} at the sample.

2.3. qDIC analysis

In order to obtain quantitative phase information, we follow the analysis described in ref. 24 and 27, briefly summarised here for clarity. The transmitted intensity image in DIC can be expressed as

$$I_t(\mathbf{r},\psi) = \frac{I_e}{2}[1-\cos(\psi-\delta(\mathbf{r}))], \quad (1)$$

with the excitation intensity I_e, the position in the sample plane $\mathbf{r}$, the phase offset ψ, and the difference $\delta(\mathbf{r})$ of the optical phase shift ϕ for the two beams that pass through the sample at two adjacent points separated by the shear vector $\mathbf{s}$. This is expressed as

$$\delta(\mathbf{r}) = \phi(\mathbf{r}+\mathbf{s}/2) - \phi(\mathbf{r}-\mathbf{s}/2). \quad (2)$$

To reduce the influence of a residual spatial dependence of I_e, which includes inhomogeneities in illumination and detection, we acquire two images at opposite angles θ of the de-Sénarmont polarizer, providing the intensities $I_\pm = I_t(\mathbf{r},\pm\psi)$ where $\psi = 2\theta$. The contrast image is then defined as

$$I_c(\mathbf{r}) = \frac{I_+(\mathbf{r}) - I_-(\mathbf{r})}{I_+(\mathbf{r}) + I_-(\mathbf{r})}. \quad (3)$$

By combining eqn (1) and (3), we obtain

$$I_c(\mathbf{r}) = \frac{\sin(\psi)\sin(\delta)}{\cos(\psi)\cos(\delta)-1} \quad (4)$$

which, for $0 \leq \psi \pm \delta \leq \pi$, can be solved analytically[27] for δ, yielding

$$\delta(\mathbf{r}) = \arcsin\left(I_c \frac{\cos(\psi)\sqrt{1-I_c^2}-1}{\sin(\psi)\left(1+I_c^2\cot^2(\psi)\right)}\right). \quad (5)$$

To extract the phase ϕ from δ, a Wiener deconvolution in the Fourier domain of wave vector $\mathbf{k}$ is used. Eqn (2) is written in the Fourier domain as

$$\mathcal{F}(\delta(\mathbf{r})) = \xi(\mathbf{k})\mathcal{F}(\phi(\mathbf{r})), \quad (6)$$

with $\xi(\mathbf{k}) = 2i\sin(\mathbf{k}\cdot\mathbf{s}/2)$ and $\mathcal{F}$ denoting the Fourier transform. Using Wiener deconvolution with a signal to noise parameter κ, we retrieve the phase using

$$\phi(\mathbf{r}) \approx \mathcal{F}^{-1}\left(\frac{\mathcal{F}(\delta(\mathbf{r}))}{\xi(\mathbf{k}) + (\kappa\xi(\mathbf{k})^*)^{-1}}\right), \quad (7)$$

where the * denotes the complex conjugation. The shear $|\mathbf{s}|$ for highest sensitivity is approximately given by the optical resolution, due to the magnitude of $\xi(\mathbf{k})$ over the $\mathbf{k}$ range of the image, $|\mathbf{k}| < 4\pi\mathrm{NA}/\lambda$. $\xi(\mathbf{k})$ is maximum for $\mathbf{k}\cdot\mathbf{s} = \pi$, which occurs at the edge of the image $|\mathbf{k}|$ range for $|\mathbf{s}| = \lambda/(4\mathrm{NA})$, yielding a shear value of 183 nm for 0.75 NA and 94 nm for 1.45 NA. Requiring instead that the condition $\mathbf{k}\cdot\mathbf{s} = \pi$ occurs in the centre of the $|\mathbf{k}|$ range results in twice these shear values. We see that the shear of the Nikon N2 DIC (238 nm) is in the range of these estimates for all objectives used.

To analyze particle volumes, the phase $\phi(\mathbf{r})$ is then spatially integrated over a circular area centred at the NP (as previously applied to extinction images[28,29]) using a dual radius method, as follows. Firstly, particle positions are determined by maxima of ϕ. The background phase for a given particle is determined as the mean phase over the area A_b within the distance r_i and $2r_i$ from the particle position, namely

$$\phi_b = {A_b}^{-1}\int_{A_b}\phi(\mathbf{r})\mathrm{d}\mathbf{r}. \quad (8)$$

The measured integrated phase A_ϕ^m over the particle is then calculated over an area A_i with a distance below r_i from the particle position, using

$$A_\phi^m = \int_{A_i}(\phi(\mathbf{r}) - \phi_b)\mathrm{d}\mathbf{r} \quad (9)$$

where $\mathrm{d}\mathbf{r}$ is the area element, $\mathrm{d}x\mathrm{d}y$ in cartesian coordinates. When considering the optical phase difference created for light of wavelength λ by a particle of refractive index n_p surrounded by a medium of index n_m, we can introduce the particle thickness $t(\mathbf{r})$, leading to a phase difference to the surrounding of

$$\phi(\mathbf{r}) = \frac{2\pi}{\lambda}(n_p - n_m)t(\mathbf{r}). \quad (10)$$

Evaluating eqn (9) for this phase difference, we find

$$A_\phi = \frac{2\pi}{\lambda}(n_p - n_m)V_p \quad (11)$$

with the particle volume

$$V_p = \int_{A_i} t(\mathbf{r})\mathrm{d}\mathbf{r} \quad (12)$$

located completely inside A_i. Therefore, V_p can be determined from A_ϕ knowing the refractive index values and the wavelength. For spherical particles, the volume is determined by their radius R_p, so that we find

$$R_p = \sqrt[3]{\frac{3\lambda A_\phi}{8\pi^2(n_p - n_m)}}. \quad (13)$$

Importantly, the measured phase area A_ϕ^m is affected by the finite spatial resolution and the finite κ in eqn (7), and has to be corrected to obtain A_ϕ, as we detail later. The software and parameters used for the analysis are described in the ESI section S8.†

3. Results and discussion

3.1. PS beads

PS beads of known radius and refractive index were used as a reference standard, to test the accuracy of NP sizing by qDIC. A representative differential phase image $\delta(\mathbf{r})$ for nominally 100 nm radius PS beads deposited onto glass and embedded in silicon oil is shown in Fig. 1a using the 1.45 NA objective and a phase offset of $\psi = 30°$ (see Methods for details of the sample and optical set-up). The corresponding images for the 0.75 NA and 1.27 NA objectives are shown in the ESI Fig. S5 and S6,† respectively. The typical shadow-cast appearance of the individual beads is observed. Note the remarkable absence of blemishes or vignetting on a scale of only ± 50 mrad, which is a result of using the DIC contrast eqn (3), as compared to individual DIC images (for illustration the I_+ image corresponding to Fig. 1a shown in the ESI Fig. S7†).

3.2. qDIC optimization and calibration

The qDIC analysis discussed in section 2.3 uses as parameters the signal to noise ratio κ in the Wiener deconvolution, and the area radius r_i to evaluate the integrals. To choose the parameter values for best precision and accuracy, the dependence of the measured integrated phase A_ϕ^m and its noise is evaluated as function of these parameters. For the discussion, let us consider here data taken on PS beads mounted in silicone oil, for the 1.45 NA microscope objective, at a phase offset of $\psi = 30°$. The data were analysed for κ ranging from 0.5 to 10^5, and r_i from 0.5 to 9 pixels. Representative images of the optical phase $\phi(\mathbf{r})$ for $\kappa = 1$, 200, and 1000 are shown in Fig. 1b–d around a single bead.

As κ is increased, the extension of spatial features along the shear direction is increasing proportional to $\sqrt{\kappa}$. This is the result of the spatial high-pass filter along the shear resulting from the Wiener filter of qDIC, eqn (7). Its cut-off wave vector

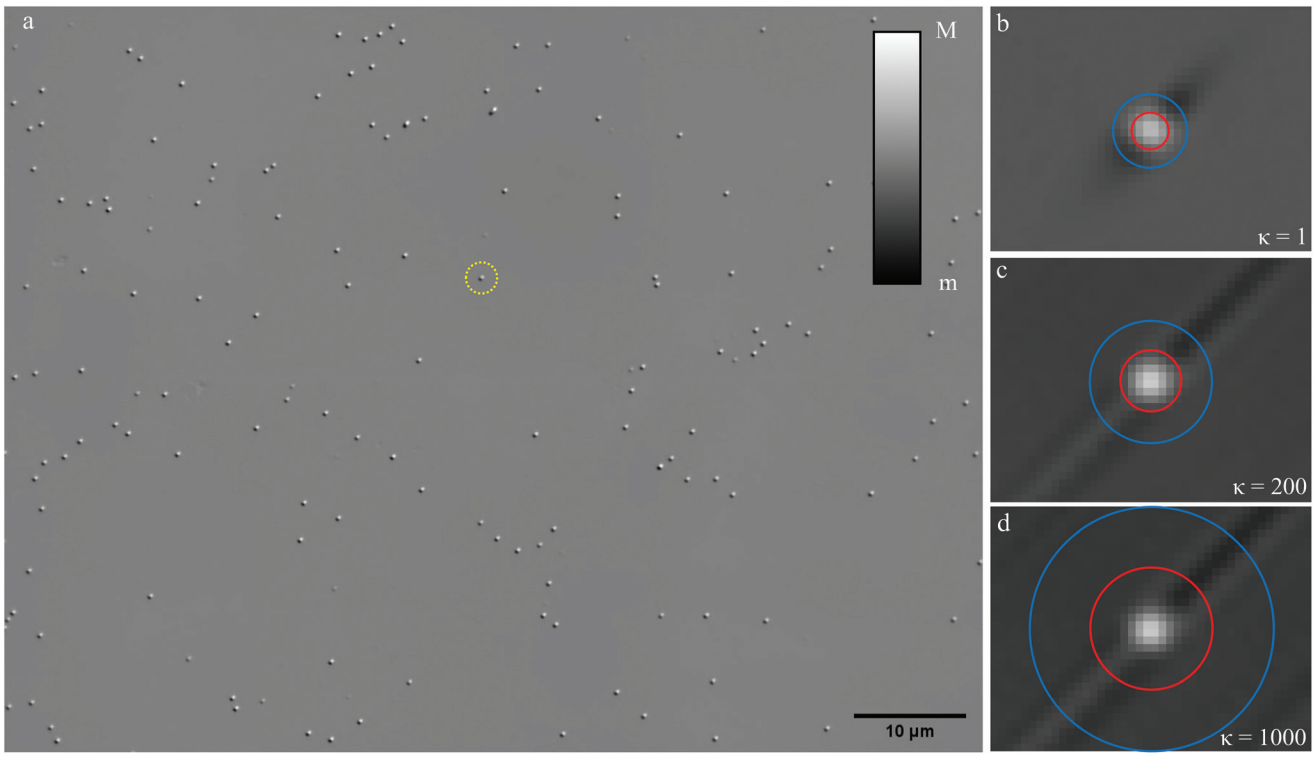

Fig. 1 qDIC microscopy on individual PS beads of nominal 100 nm radius, drop cast onto glass and surrounded by silicon oil, imaged with a 1.45 NA objective and a phase offset of ψ = 30°. (a) $\delta(\mathbf{r})$ on a grey scale as shown, from m = −50 mrad to M = 50 mrad. The shadow cast impression is evident, with the shear $\mathbf{s}$ = 0.16(1,1) µm in the (x,y) coordinates (x is the horizontal axis and y the vertical in the image). Optical phase maps $\phi(\mathbf{r})$ showing a region of (2.71 × 2.07) µm^2 around a selected bead indicated by the dashed circle, for κ = 1 (b, m = −15 mrad to M = 30 mrad), κ = 200 (c, m = −20 mrad to M = 40 mrad), and κ = 1000 (d, m = −30 mrad to M = 30 mrad). The red and blue circles have the radii r_i and $2r_i$, respectively, with r_i = 2.5, 4, 8 pixels in (b), (c), (d), respectively, representing different integration areas A_i and A_b used in the analysis for eqn (8) and (9).

$\mathbf{k}_c$ is given by the condition $\kappa|\xi(\mathbf{k}_c)|^2 = 1$, which for small $|\xi|$ is approximated by $|\mathbf{k}_c \cdot \mathbf{s}|\sqrt{\kappa} = 1$, so that $|\mathbf{k}_c|$ is proportional to $1/\sqrt{\kappa}$. While allowing for longer range features to be retrieved, increasing κ also increases the noise due to the larger amplification of the data by the filter function for small $|\xi|$.

Notably, the stripes show here a triplet structure, which is attributed to the asymmetry of the point-spread function for linearly polarised light. As the two sheared components have linear polarization along and across the shear, their spatial elongation is oriented also in this way, resulting in accordingly different shapes of the probed regions. For smaller NA, this asymmetry is reduced, and with it the triplet structure, as can be seen in the results for the 0.75 NA objective in Fig. S5.†

The radius r_i instead determines the size of the circular areas A_i and A_b over which the integrals of the optical phase are calculated (eqn (8) and (9)), as shown by the red and blue circles in Fig. 1b–d. For r_i larger than the cut-off of the Wiener filter, A_i contains also regions of inverted (negative) contrast (see dark tails in Fig. 1b–d), reducing the resulting A_ϕ^m. On the other hand, for r_i smaller than the spatial resolution, A_i will not contain the full response and again A_ϕ^m will be reduced. Furthermore, the areas scale with r_i^2, so that the shot-noise in A_ϕ^m will scale with r_i, favouring small r_i for high signal to noise ratio (SNR).

The evaluated A_ϕ^m as function of κ and r_i is given in Fig. 2a for the bead selected in Fig. 1. We find, in accordance with the above qualitative arguments, that A_ϕ^m is increasing steeply with r_i up to about 4 pixels, which is the size of the point-spread function (PSF) (see red circle in Fig. 1c). For larger r_i, A_ϕ^m

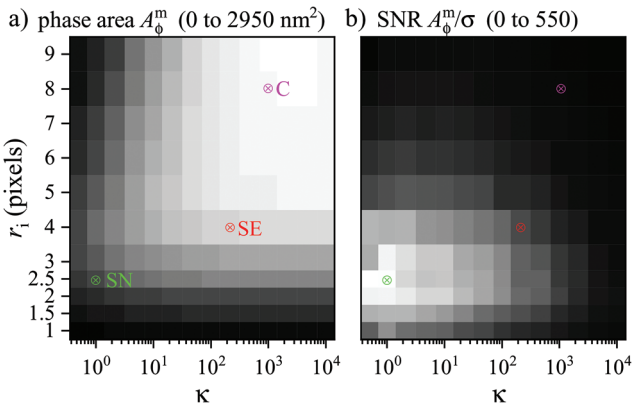

Fig. 2 Phase area A_ϕ^m (a, m = 0 to M = 2950 nm^2) and SNR A_ϕ^m/σ (b, from m = 0 to M = 550) as function of κ and r_i for a PS bead in silicon oil imaged with the 1.45 NA objective and a phase offset of ψ = 30° as in Fig. 1. The chosen (κ, r_i) pairs SN, SE, and C are indicated.

reduces for small values of κ, and increases for large κ, converging to a stable value for $\kappa > 500$ and $r_i > 7$.

We define three (κ,r_i) pairs according to the following criteria: the pair that provides the highest SNR (called SN pair), the one for which A_ϕ^m converges to the highest value (called C pair), and a compromise choice which still gives a good SNR but has a reduced systematic error due to a lower sensitivity to the specific shape of the PSF (called SE pair). Based on Fig. 2a, as C pair we use (κ, r_i) = (1000, 8), where the units of r_i are pixels (one pixel has a size of 65 nm on the sample for these data). To choose the SN pair, we determine the SNR by evaluating A_ϕ^m at positions not showing a visible particle in the image, and fit its histogram with a Gaussian to determine its standard deviation σ, as can be seen in the ESI Fig. S1.† The r_i dependencies of A_ϕ^m and σ are shown in Fig. S4† for κ = 1000. For small r_i, σ scales with r_i, as expected from shot noise, while for larger r_i, we find that σ scales with r_i^2, indicating the dominance of background structure. The resulting SNR A_ϕ^m/σ corresponding to Fig. 2a is given in Fig. 2b. We find that the SNR is increasing with r_i up to about 2 pixels. This can be understood considering that for small r_i, A_ϕ^m is scaling with r_i^2, while σ scales only with r_i. For larger r_i instead, A_ϕ^m is saturating or even decreasing, as seen in Fig. 2a, so that the SNR decreases, due to the increasing σ. Moreover, for κ above 2, for which the Wiener filter cut-off is larger than the PSF, the SNR is decreasing as expected from the qualitative arguments mentioned previously. The highest SNR is obtained for the SN pair (1, 2.5). Finally, for the SE pair we chose a larger r_i corresponding to the PSF size, and accordingly the κ giving the highest SNR, which is (200, 4). This choice reduces systematic errors observed for lower r_i, as will be shown later.

Note that the values of κ and r_i for the SN, SE, and C pairs depend on the objective and tube lens used, which determine the optical resolution. We report in the ESI† A_ϕ^m as function of κ and r_i for the 0.75 NA and 1.27 NA objectives, see Fig. S2a and S3a,† with the corresponding SNR A_ϕ^m/σ, see Fig. S2b and S3b,† and the resulting parameters for the SN, SE, and C pairs.

3.3. Correction factors and polystyrene bead radii

Since the SN and SE pairs provide a phase area A_ϕ^m which is lower than the converged value given by the C pair, we determine correction factors ρ for these pairs to scale A_ϕ^m to the converged value representing A_ϕ (see also eqn (9) and (11)). To do this, each particle's A_ϕ^m for the C pair was divided by the value for the SN or SE pair, and the histogram of the resulting ratios was fitted with a Gaussian distribution, to determine center and standard deviation. The distribution obtained for the PS beads mounted in silicone oil imaged using the 1.45 NA objective is shown in Fig. 3 for both the SN and SE pair, resulting in correction factors of $\rho = 3.48 \pm 0.27$ and $\rho = 1.25 \pm 0.07$, respectively. The correction factors found for the different optics and corresponding SE and SN pairs are given in Table 1. Notably, the relative standard deviation of correction factors is generally larger for the SN than the SE pair, showing a reduced systematic error for the SE pair. We emphasize that the correction factors for a given pair (κ, r_i) depend only on the optical

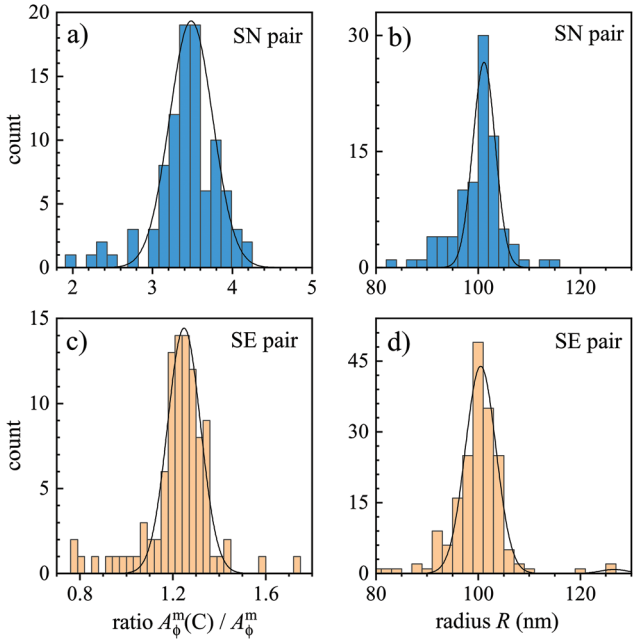

Fig. 3 Analysis of PS beads in silicon oil measured using the 1.45 NA objective and a phase offset of $\psi = 30°$ as in Fig. 1. (a and c) Histogram of the ratio of A_ϕ^m for the (κ,r_i) pair C to A_ϕ^m for pair SN (a) or SE (c), with Gaussian fits yielding the mean correction factor ρ. (b and d) Histograms of the resulting bead radii R, for the SN (b) and SE (d) pair.

setup, and not on the particles investigated, and are therefore valid for any dielectric particle which is smaller than the PSF.

The mean correction factor was then used to define the phase area $A_\phi = \rho A_\phi^m$, which in turn determines the particle volume and corresponding radius from the measurements. Histograms of the resulting radii for the SE and SN pairs are shown in Fig. 3b and d. Note that the C pair, while not requiring a correction factor, corresponds to the lowest SNR of the three pairs, about 20 for the 1.45 NA objective. The noise in the C pair is the dominant contribution to the standard deviation of the measured correction factor for the SE pair. The error of the mean correction factor, considering the roughly 100 particles analysed, is roughly 10 times smaller than the standard deviation, resulting in a relative error below 1%.

To find the mean particle size and standard deviation for each measured radius distribution, the following fit function was used, given by a sum of Gaussian distributions to account for particle aggregates:

$$p(R) = \sum_{n=1}^{8} \frac{B_n}{\sigma_n \sqrt{2\pi}} \exp\left(\frac{-(R - R_n)^2}{2{\sigma_n}^2}\right), \qquad (14)$$

where $R_n = R_1 n^{1/3}$ is the mean radius of an n-particle aggregate, and $\sigma_n = \sigma_1 n^{-6/2}$ is the standard deviation of this radius, assuming an independent radius variation of the individual particle in the aggregate (a derivation of R_n and σ_n is shown in

Table 1 qDIC results for PS beads: correction factors ρ, particle integrated phase area A_ϕ and radii R with standard deviations, as well as shot noise σ_s and background noise σ_b. Results for each investigated combination of mounting medium, objective NA, phase offset ψ, and analysis pair are shown. The radius limit was calculated from σ_b using eqn (13) and $A_\phi = \rho\sigma_b$

ψ	NA	Pair	κ	r_i	ρ	A_ϕ (nm^2)	R (nm)	σ_s (nm^2)	σ_b (nm^2)	Radius limit (nm)
Silicone oil $n_{so} = 1.518$										
30	0.75	SN	1	1	7.07	3193.4	97.5 ± 4.30	62.0 ± 1.3	2.05 ± 0.32	16
		SE	100	2	1.27	3164	97.2 ± 4.5	634.7 ± 4.7	50.39 ± 0.85	27
	1.27	SN	1	1.5	3.76	3466.1	100.2 ± 4.4	13.61 ± 0.41	0.62 ± 0.09	8.8
		SE	100	2	1.63	3539.3	100.9 ± 3.5	110.7 ± 2.6	9.36 ± 0.44	16
	1.45	SN	1	2.5	3.48	3570.9	101.2 ± 2.2	17.9 ± 1.0	1.94 ± 0.17	13
		SE	200	4	1.25	3497.3	100.5 ± 3.0	131.3 ± 5.1	16.66 ± 0.87	18
60	0.75	SN	1	1	7.07	4045.7	105.5 ± 5.7	121.5 ± 3.9	3.9 ± 1.0	20
		SE	100	2	1.27	3518.2	100.7 ± 3.4	1250.6 ± 10.5	58.6 ± 2.1	28
	1.27	SN	1	1.5	3.76	2907.6	94.5 ± 4.1	28.11 ± 0.55	0.46 ± 0.25	7.9
		SE	100	2	1.63	3105.8	96.6 ± 4.2	235.3 ± 6.5	10.1 ± 1.4	17
	1.45	SN	1	2.5	3.48	3549.8	101.0 ± 2.3	31.21 ± 0.50	1.53 ± 0.10	12
		SE	200	4	1.25	3486.9	100.4 ± 2.5	215.1 ± 8.8	18.4 ± 1.5	19
90	0.75	SN	1	1	7.07	4011.3	105.2 ± 5.4	212 ± 13	0.0 ± 5.4	22
		SE	100	2	1.27	3507.8	100.6 ± 4.4	2222 ± 30	77.2 ± 7.3	31
	1.27	SN	1	1.5	3.76	2639	91.5 ± 4.2	49.17 ± 0.55	1.17 ± 0.18	11
		SE	100	2	1.63	2735.7	92.6 ± 4.7	375.4 ± 3.9	14.14 ± 0.91	19
	1.45	SN	1	2.5	3.48	3645.5	101.9 ± 2.1	51.1 ± 1.8	2.27 ± 0.38	13
		SE	200	4	1.25	3602.8	101.5 ± 2.5	361 ± 13	24 ± 24	21
Water immersion oil $n_{wo} = 1.334$										
30	0.75	SN	1	1	6.75	13 000.1	102.0 ± 4.3	61.8 ± 1.4	4.00 ± 0.24	13
		SE	100	2	1.23	12 434.9	100.5 ± 2.5	644 ± 17	91.9 ± 3.0	21
	1.27	SN	1	1.5	5.26	12 103.9	99.6 ± 4.2	24.03 ± 0.54	1.56 ± 0.09	8.7
		SE	100	2	2.12	11 922.5	99.1 ± 3.7	106.94 ± 0.86	10.52 ± 0.14	12
	1.45	SN	1	2.5	4.12	12 472.1	100.6 ± 5.5	15.98 ± 0.37	1.45 ± 0.06	7.9
		SE	200	4	1.38	12 711.7	101.2 ± 4.3	139 ± 45	17.7 ± 7.2	13
60	0.75	SN	1	1	6.75	12 031.1	99.4 ± 3.6	122.3 ± 3.8	4.66 ± 0.88	14
		SE	100	2	1.23	10 940.2	96.3 ± 2.8	1276 ± 14	100.0 ± 2.4	22
	1.27	SN	1	1.5	5.26	10 838.3	96.0 ± 5.1	50.6 ± 1.4	2.07 ± 0.29	9.6
		SE	100	2	2.12	11 008.5	96.5 ± 4.5	227.7 ± 3.4	11.83 ± 0.65	13
	1.45	SN	1	2.5	4.12	14 019.8	104.6 ± 5.6	32.43 ± 0.80	1.56 ± 0.16	8.1
		SE	200	4	1.38	15 431.8	108.0 ± 4.2	233 ± 12	18.7 ± 2.0	13
90	0.75	SN	1	1	6.75	11 145.9	96.9 ± 4.2	197.2 ± 6.5	3.1 ± 3.1	12
		SE	100	2	1.23	10 272.6	94.3 ± 2.9	2108 ± 61	141 ± 11	24
	1.27	SN	1	1.5	5.26	11 249.8	97.2 ± 5.4	86.8 ± 3.6	2.5 ± 1.1	10
		SE	100	2	2.12	11 284.6	97.3 ± 4.6	395 ± 13	11.8 ± 3.5	13
	1.45	SN	1	2.5	4.12	14 923.1	106.8 ± 4.4	53.8 ± 1.7	2.39 ± 0.35	9.3
		SE	200	4	1.38	14 425.7	105.6 ± 5.7	370 ± 13	27.2 ± 2.2	15

the ESI†). Furthermore, for a Poisson distribution of particle numbers in the aggregates, we have

$$B_n = B\frac{\lambda^n e^{-\lambda}}{n!}, \quad (15)$$

with a normalization B and the average number λ of particle per aggregate. Note that λ includes the $n = 0$ probability, which is not part of the analyzed particles. Fits are shown in Fig. 3b and d, yielding the parameters $R_1 = 101.2$ nm, $\sigma_1 = 2.2$ nm, and $\lambda = 0.01$ for the SN pair, and $R_1 = 100.5$ nm, $\sigma_1 = 3.0$ nm, and $\lambda = 0.03$ for the SE pair. Note the quantitative agreement between the measured PS bead radius and the size provided by the manufacturer within the specified standard deviation. This shows the accuracy of the method, as further discussed later in subsection 3.5. Histograms of the correction factors and radii for PS beads in different mounting media and for the various objectives used are shown in the ESI (Fig. S15 to S19†), with the resulting bead radii $R = R_1 \pm \sigma_1$ summarised in Table 1.

3.4. Background and shot noise

To characterise the precision of the method, we evaluated the error derived from the noise in the measurements. The noise in the qDIC δ images in the absence of strong contrast, that is for $I_c \approx 0$, consists of two components. Firstly, the photon shot noise in the measured images $I_\pm$, which depends on the average number of detected photoelectrons (phe) per pixel N_e. For an acquisition consisting of N_a frames which are averaged, the shot noise is $\sigma_c = 1/\sqrt{2N_eN_a}$ in the DIC contrast I_c (where the factor $1/\sqrt{2}$ accounts for the use of two images in I_c, see eqn (3)). For typical values used in our work, $N_e = 10^4$ and $N_a = 256$, we find σ_c

= 0.04%, and for a single frame σ_c = 0.7%. To evaluate the corresponding noise σ_δ of δ, which is related to I_c by eqn (4), we find

$$\sigma_c = \sigma_\delta \left|\frac{dI_c}{d\delta}\right|_{\delta=0} = \sigma_\delta \left|\frac{\sin(\psi)}{1-\cos(\psi)}\right|. \quad (16)$$

We can see that for small offset angles $0 < \psi \ll 1$, σ_δ is reduced, by a factor of about $\psi/2$ compared to the noise for ψ = 90°, as discussed previously.[26] However, smaller ψ also reduces the range which can be retrieved, and the transmitted intensity (eqn (1)) is reduced, requiring longer measurement times or stronger illumination. Furthermore, the non-ideal optical elements used (finite extinction of the polarizers, non-perfect matching of the DIC prisms, birefringence of the objective due to residual strain and oblique transmission) results in deviations of the measured data from the ideal behaviour given by eqn (1). Most notably, in high-quality objectives as used here, light rays incident at large oblique angles, collected and collimated by the objectives, are also at oblique incidence on the lens surfaces of the objectives. The resulting polarization dependent transmission of s and p polarized waves provides a variation of the polarization of the collimated ray after the objective, which depends on its incident direction. As a consequence, the rays are not completely blocked by the polarizer, and a significant transmission at ψ = 0 can be observed also without sample.

This issue has been identified early on in polarization microscopy,[30] and a recent calculation of the diattenuation and phase shift for a 1.27 NA objective can be found in ref. 31. It has also been shown that the polarization mixing can be reduced by a polarization rectifier, and a reduction of the background from 0.2% to 0.01% for a 1.25 NA objective was shown.[32] A more recent discussion including results from a liquid crystal rectifier is given in ref. 33. However, presently such rectifiers are not offered by manufacturers of microscope objectives. We note that the objectives used in our work have an apochromatic and aplanatic performance and high transmission across a wide wavelength range (435–850 nm), constraining the lens design including the anti-reflex coatings. We can thus assume that a given value for the upper limit of the polarization mixing is one of the lens design goals. When limiting the detection and excitation to a single optical mode in confocal microscopy, a complete extinction can in principle be achieved using polarization compensation.[34] Notably, 10^{-8} extinction has been shown[35] and a discussion of remaining limits in a model setup reaching 10^{-9} is given in ref. 36. We emphasize that in DIC additionally a mismatch of their shear of the two Nomarski prisms and a mismatch of their axial position from the conjugated planes can contribute to the finite background.

We have quantified the background transmission as a fraction η of I_e, which was found to be η = 0.80%, 0.64%, and 0.86% for the 1.45 NA, 1.27 NA, and 0.75 NA objectives, respectively. Notably, for the smallest ψ used in this work, *i.e.* 30°, the transmission (eqn (1)) is only 6.7% of I_e, so that the background constitutes a significant fraction of the ideal transmission without sample. To correct for this residual transmission (*i.e.* non perfect extinction) in the analysis, we have subtracted this background from the measured intensities $I_\pm^m$ to determine $I_\pm$. This equates to using $I_\pm = I_\pm^m - \langle I_\pm^m \rangle 2\eta/(1 - \cos(\psi))$ in eqn (3), where $\langle . \rangle$ denotes the spatial average.

Other than shot-noise, we have random structures in our samples unrelated to the particles of interest (POI). Notably, the samples that we study consist of a glass coverslip with attached particles, embedded in an immersion oil. We are imaging the glass-immersion oil interface, while other interfaces are out of focus by at least 10 μm, making them essentially invisible in DIC. Therefore, the background in the absence of POIs originates from unwanted structures at the glass – immersion oil interface. It is thus paramount to use high-quality coverslips and clean them properly before attaching the POIs (see sample preparation protocol in Methods section). Even after cleaning, however, there is a remaining surface roughness of a few nanometers which is an intrinsic feature of glass surfaces fabricated by float techniques, due to the thermally excited surface waves at the glass transition during cooling. Since in DIC the contrast at the interface scales with the refractive index difference between glass and immersion oil, optically clearing the interface by matching the refractive indices is an effective way to suppress background from surface roughness. The two immersion oils used in the present work have an index difference to glass of about 0.2 (water oil) and <0.002 (silicone oil). Thus, when using silicon oil, surface roughness is not relevant.

To unpick the background and shot noise contributions, we determine the noise in A_ϕ^m using 1000 points in regions without evident PS beads, which were then analysed with the SN and SE pairs. A Gaussian function was fitted to the resulting integrated phase area distribution to determine its standard deviation σ. An example of this histogram is shown in the inset of Fig. 4, and the resulting σ is shown in Fig. 4 as function of N_a for the 1.45 NA objective on the sample in silicone oil and phase offsets of ψ = 30, 60, and 90°. We find a decreasing σ with increasing N_a, as expected for shot noise, which tends to saturate for N_a > 100, indicating the background noise limit. We fit this dependence as

$$\sigma = \sqrt{\frac{\sigma_s^2}{N_a} + \sigma_b^2}, \quad (17)$$

where σ_s is the shot-noise for a single frame, and σ_b is the background noise due to sample inhomogeneities. The resulting σ_s and σ_b are given in Table 1. Similar plots for the other objectives and immersion oils are shown in the ESI Fig. S20 to S24.†

Recalling the scaling of the noise given in eqn (16), we fitted the dependence of the resulting σ_s for the SN pair with the phase offset ψ (see Fig. 5) using

$$\sigma_s = \sigma_{s0} \left|\frac{1-\cos(\psi)}{\sin(\psi)}\right|, \quad (18)$$

where σ_{s0} is the noise for ψ = 90°, the phase offset with the largest retrieval range in eqn (5). We find a good fit with σ_{s0} =

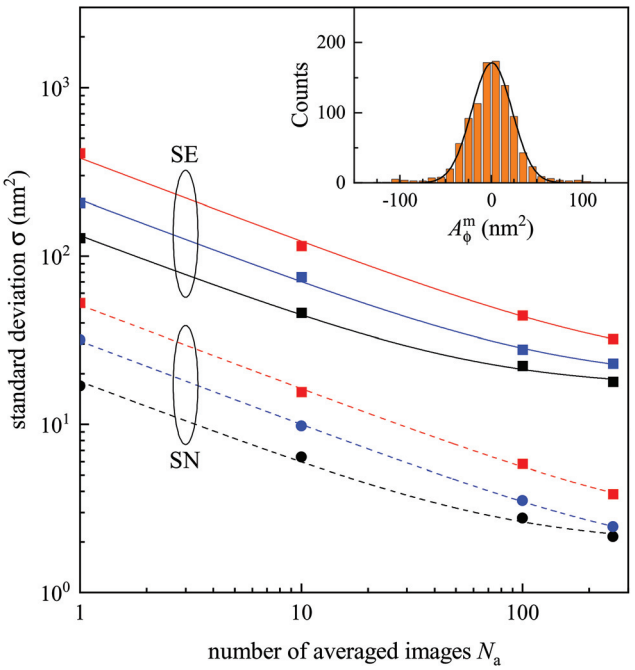

Fig. 4 Standard deviation σ, from the distribution of A_ϕ^m in regions of the sample without PS beads, *versus* number of averages N_a, for PS beads mounted in silicone oil imaged using the 1.45 NA objective and phase offsets ψ of 30° (black), 60° (blue), and 90° (red). The inset shows the histogram of A_ϕ^m for N_a = 100, analysed using the SE pair imaged at ψ = 30°, and the fitted Gaussian distribution (black line).

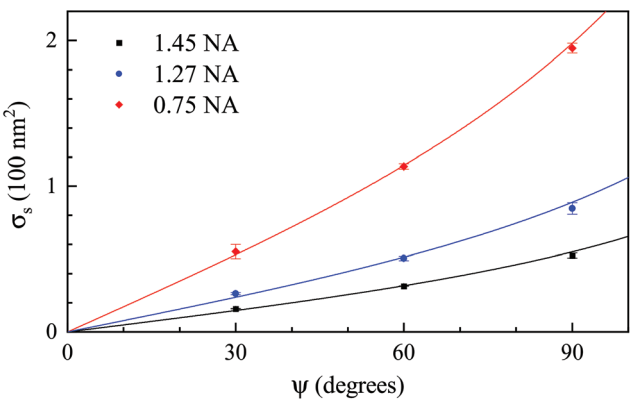

Fig. 5 Single frame shot-noise σ_s of A_ϕ^m for the different objectives and phase offset angles, ψ, when analysed using the corresponding SN pair. The lines are fits using eqn (18).

55, 89, and 198 nm² for the 1.45 NA, 1.27 NA, and 0.75 NA objectives, respectively.

As can be seen in Table 1, the smallest single frame shot noise σ_s is found for the 1.27 NA objective and SN pair for beads in silicon oil, yielding about 14 nm². Using eqn (11) (and taking into account the correction factor ρ to scale the phase area), this corresponds to a PS bead of 25 nm radius. For samples in water oil, σ_s is 16 nm² using the 1.45 NA objective, corresponding to a PS bead radius of 17.5 nm as sensitivity limit from shot noise with a single frame acquisition. Generally, σ_s decreases with (i) increasing NA due to the improving spatial resolution, (ii) going from the SE to the SN pair due to the better SNR (Fig. 2), (iii) decreasing phase offset due to the increased contrast (eqn (16)). The size limit scales with the third root of the noise, and decreases going from silicone to water oil due to the increased refractive index difference (eqn (11)).

Ultimately, for a sufficient number of frames N_a, the shot-noise can be decreased to a point where the background noise σ_b limits the sensitivity. An overview over the measured σ_b is given in Fig. 6. On some occasions, and specifically for the 0.75 NA having a larger σ_s, an increase of σ_b with ψ is seen, which is not expected, and is attributed to a systematic error; see also the fits in Fig. 4. We note the reduction of σ_b going from the SE to the SN pair by a factor of 10 to 20. Interestingly, σ_b for the two immersion oils is generally quite similar, even though the water oil has much larger refractive index difference to the glass substrate than silicone oil. This indicates that glass substrate roughness is not the dominant background, suggesting that it is instead due to other impurities, *e.g.* remaining debris upon sample preparation.

For ψ = 30°, the SN pair, and the 1.27 NA objective, σ_b = (0.62 ± 0.06) nm² for silicone oil, corresponding to a smallest detectable bead radius of 8.8 nm. For samples immersed in water oil instead, we find σ_b = (1.56 ± 0.06) nm² and a smallest detectable bead radius of 8.7 nm. Such similar radii would be expected if σ_b would be caused by dielectric debris on the surface of a refractive index similar to the one of PS.

Other quantitative phase contrast techniques have a reported uncertainty of 0.3 to 2 nm in optical path length.[20] Using a wavelength of 550 nm and a point-spread function size of 300 nm, this corresponds to an uncertainty in A_ϕ of 308–2056 nm², and thus a radius limit for PS beads in water of 32 to 60 nm. Notably, the radius limit in the present work is about 5 times lower.

It should be noted that the iSCAT technique[11] avoids the static background noise σ_b by analyzing particles which attach and/or detach during measurements, so that the difference

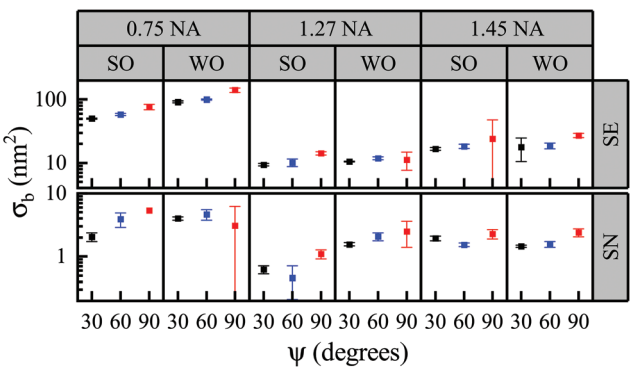

Fig. 6 Overview of the background noise σ_b for different phase angles ψ, objectives 0.75, 1.27, and 1.45 NA, water oil (WO) and silicone oil (SO) immersion, and analysis pairs SE and SN.

can be detected. Such a method can also be applied to qDIC, resulting in a sensitivity only limited by the shot-noise. For example, using the 1.45 NA objective, samples in water oil, ψ = 30°, the SN pair, and N_a = 1000 acquisitions, the radius limit (scaling with $N_a^{-1/6}$) is down to 3.8 nm, which can be achieved within 1 s with a modern camera. We also note that by reducing the phase offset, the sensitivity can be increased, see eqn (16). Assuming ideal optics and η = 0, we find that for ψ = 1° the limit for N_a = 1000 is a radius of 1.8 nm.

3.5. PS bead sizes

Samples with PS beads as described in section 1 were measured and the resulting A_ϕ was converted into a PS volume, using the refractive index of n_p = 1.59. Note that this index can vary depending on the packing density of the PS. Hence, rather than assuming a nominal value, we have determined the refractive index for the PS beads used here, by considering the measured change of the DIC contrast *versus* immersion medium index, as discussed in the ESI section S2.†

The retrieved particle radii, using PS beads in silicone oil and the 1.45 NA objective, are shown in Fig. 3 for the SE and SN pairs. The histograms were fitted with eqn (14) yielding (R_1 ± σ_1) = (101.2 ± 2.2) nm and (100.5 ± 3.0) nm, respectively, as mentioned previously and summarised in Table 1. Results for other objectives and immersion oils are also given in Table 1, with the histograms shown in the ESI Fig. S15 to S19.† Importantly, we find a quantitative agreement of the measured radii for all immersion oils, objectives, and phase offset combinations within a few %.

The smallest σ_1 is found using the 1.45 NA objective with beads in silicone oil and for the SN pair, which gives a relative variation of σ_1/R_1 = 2.2%, consistent with the cv below 3% specified by the manufacturer. This suggests that the contribution of the measurement noise to the uncertainty in the size distribution is negligible. The influence of the measurement noise σ to the size distribution can also be calculated, and in turn removed, resulting in a corrected σ_1^c given by

$$\sigma_1^c = \sigma_1 \sqrt{1 - \left(\frac{\sigma}{\sigma_1^A}\right)^2}, \tag{19}$$

where σ_1^A is the noise in A_ϕ^m corresponding to σ_1. Using eqn (13) this is given by

$$\sigma_1^A = \sigma_1 \frac{\partial A_\phi^m}{\partial R} = \sigma_1 \frac{8\pi^2 R^2 (n_p - n_m)}{\lambda \rho}, \tag{20}$$

where ρ is the mean correction factor and R is the mean radius R_1. It was found that the influence of the measurement noise on σ_1 was negligible, for all objectives and both the SN and SE pairs. For the case of PS beads mounted in silicone oil, imaged using the 1.45 NA objective at ψ = 30°, σ_1 was found to be 3.0 nm for the SE pair and 2.2 nm for the SN pair. The calculated σ_1^c for these cases were found to be 2.9 nm and 2.2 nm for the SE and SN pairs, respectively.

As detailed in the ESI section S3 i,† the bead diameter of the batch used was measured with transmission electron microscopy (TEM) to be 187 nm, with a cv of 2.1%. Scanning electron microscopy (SEM) gave a diameter of 190 nm, dynamic light scattering (DLS) resulted in 183 nm diameter, and atomic force microscopy (AFM) gave a height of 179 nm with a cv of 3.7%. The most reliable result is SEM, since measurements were performed over a large number of beads (see ESI Fig. S9†), giving 95 nm radius, which is consistent with the qDIC results (see Table 1). The about 5% difference in radius found in qDIC compared to SEM corresponds to a 15% difference in the qDIC phase area. This is consistent with the accuracy of determining the saturated A_ϕ^m for the C pair seen in Fig. S4a.† A systematic variation of about 5% is also seen between the different objectives and pairs, which each have their own correction factor.

3.6. Small PS beads

To demonstrate the capability of the technique to measure small PS particles, fluorescent PS beads of nominally 15 nm radius were examined. Here a 100 × 1.49 NA apochromat objective (part number MRY10059) was used, keeping the SN pair and correction factor of the 1.45 NA objective. Its background transmission η has been determined to 0.96% (see Table S1†). A phase offset of ψ = 20° was used, providing a low σ_s.

The measured phase $\phi(\mathbf{r})$ of a representative region of a sample using silicone oil is shown in Fig. 7a. Analysis of this data with the SN pair shows a phase area A_ϕ^m with a noise of σ = 1.6 nm^2, and the dependence on N_a is described by eqn (17) with σ_s = 13.3 ± 0.8 nm^2 and σ_b = 1.4 ± 0.1 nm^2. The inset shows a bead clearly visible above background, having a phase area corresponding to 24 nm radius.

The histogram of background and particle A_ϕ^m is shown in Fig. 8a. To reliably distinguish particles above background, we require that $A_\phi^m > 4\sigma$ (see grey shaded region in Fig. 8a), which in the absence of particles occurs with a probability of $p = 3 \times 10^{-5}$ for a Gaussian background distribution. Considering a spatial resolution of about s = 300 nm, this probability corresponds to an average distance of $s/\sqrt{p}$ = 53 μm between noise-induced particle detections, or about two detections over the region shown in Fig. 7a. The retrieved particle radius distribution is given in Fig. 8b. The 4σ limit corresponds to a radius of 18 nm. The distribution is decaying above this radius, as expected from the nominally 15 nm radius beads.

Importantly, the fluorescence of the beads provides an independent reporter of the bead position, and even an estimate of bead size assuming that the fluorescence intensity I_{fl} is proportional to the bead volume. We have therefore imaged the fluorescence of the same region, as shown in Fig. 7b. A good correlation between the particles visible in $\phi(\mathbf{r})$ and in $I_{fl}(r)$ can be seen, including the particle in the inset. For each particle identified in $\phi(\mathbf{r})$, the integrated fluorescence A_{fl} was determined using the same double radius method as for A_ϕ^m, but in area units of pixels, and counts converted to photoelectrons, and is shown in Fig. 8a. We can see a linear correlation of A_{fl} and A_ϕ^m, consistent with the fluorescence intensity I_{fl} being proportional to the particle volume. However, a significant spread of the proportionality is observed, which could

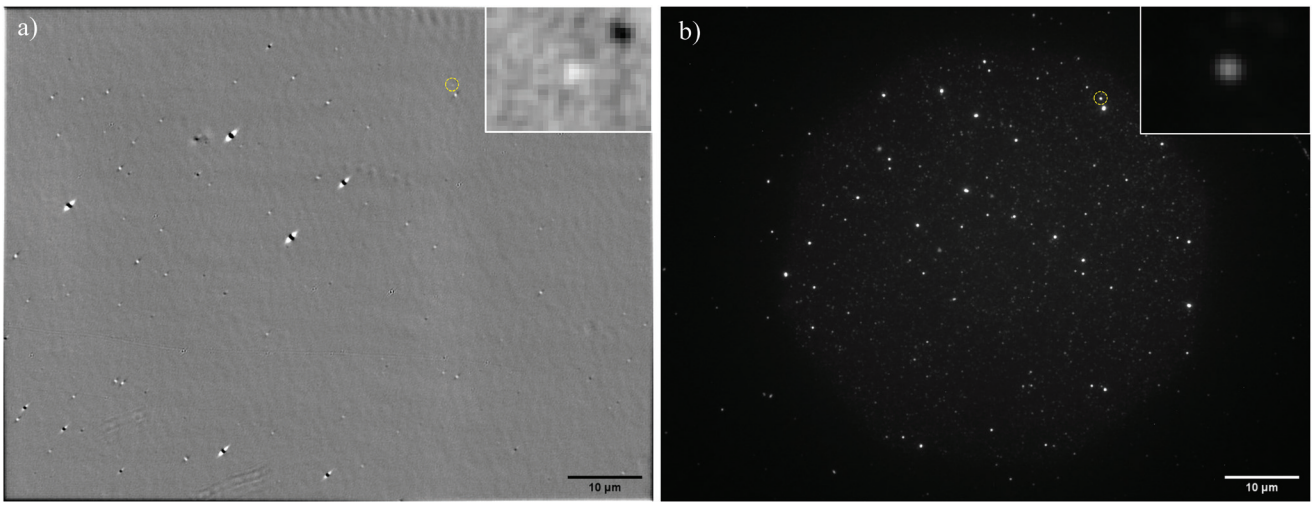

Fig. 7 (a) qDIC phase $\phi(\mathbf{r})$ on fluorescent PS beads of nominally 15 nm radius, drop cast onto glass and surrounded by silicone oil, imaged with a 1.49 NA objective at a phase offset of ψ = 20° and analyzed using κ = 1 and N_a = 256. Grey scale from m = −1 mrad to M = 1 mrad. The inset shows a region of (2.07 × 1.55) µm^2 around a bead highlighted by the yellow dashed circle, on a greyscale from m = −0.4 mrad to M = 0.4 mrad. This bead has an A_ϕ^m corresponding to a radius of 24 nm. (b) *epi*-Fluorescence intensity I_{fl} (average of 5 frames with 3 s exposure time each) of the same sample region, on a greyscale from m = 37 to M = 4177 phe. The excitation area was limited to the discernible disk region by a field aperture. Inset as in (a), greyscale m = 41 to M = 1647 phe.

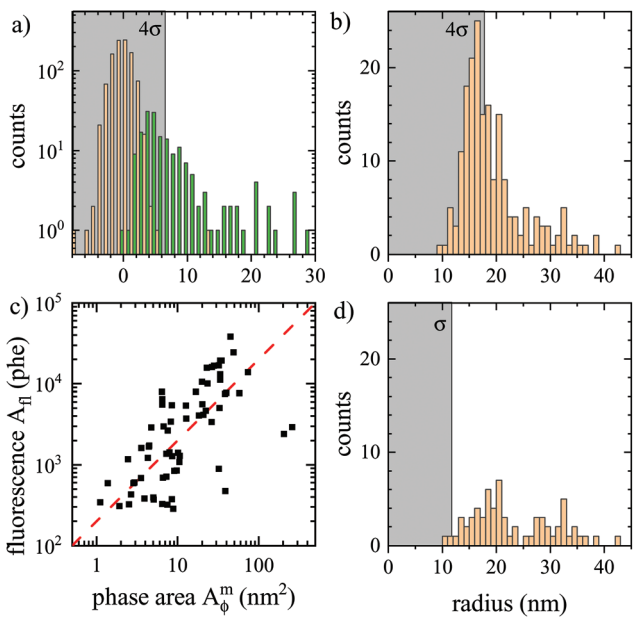

Fig. 8 Analysis of data shown in Fig. 7. (a) histogram of the phase area A_ϕ^m for background (orange, σ = 1.6 nm^2), and particles (green) located as maxima in $\phi(\mathbf{r})$ above 0.13 mrad. The region below 4σ is indicated in gray. (b) resulting histogram of particle radius. (c) fluorescence photoelectrons A_{fl} *versus* A_ϕ^m, with a proportionality indicated as dashed line. (d) Histogram of particle radius with corresponding A_{fl} above 274 phe.

be an intrinsic property of the PS beads. Notably we found that the beads lose their fluorophores over a timescale of a few hours when immersed in oil (possibly due to the missing surface tension of water allowing for swelling and solubility of the fluorophores in oil). The histogram of particles having a corresponding A_{fl} above a threshold of four standard deviations of the background in A_{fl} is given in Fig. 7d. It shows a similar distribution as the original one, but fewer particles, specifically with radii below 20 nm. This is attributed to the limitation of the analysed region to the fluorescence excitation area, and the loss of fluorophores reducing the fluorescence of small beads to below the threshold.

We have performed a similar analysis using water oil immersion, with results shown in the ESI Fig. S25 and Fig. S26.† Interestingly, the detection limit is similar to the one seen for silicone oil immersion, even though the index contrast to PS has increased by a factor of 3.56. However, the index contrast to glass has increased by a factor of about 100 and the glass roughness is clearly visible in the background structure, indicating it to be the limiting factor in this case.

As detailed in the ESI section S3 ii,† the bead diameter distribution of the batch used was measured with DLS to have a z-mean of 24 nm and a cv of 52%, while the height distribution was measured by AFM to have a mean of 16 nm with a cv of 42%. This shows that these beads have a wide distribution of sizes, consistent with the above qDIC results. Notably, the large number of particles below 20 nm diameter likely contribute to σ_b in the measured samples, while particles above 36 nm diameter can be reliably identified and measured using only qDIC.

3.7. Nanodiamond volume measurement

To showcase the method with an application example, we measured the size of individual nanodiamonds, specified by the manufacturer to have a broad distribution of sizes below 50 nm, 150 nm, and 250 nm (see also Methods section). NDs were embedded in silicon oil. Particles with nominal diameter

ranges (0–250) nm and (0–150) nm were measured using the 0.75 NA objective, while those with (0–50) nm diameters were imaged with the 1.27 NA objective (examples of the $\delta(r)$ and $\phi(\mathbf{r})$ images for each are shown in the ESI Fig. S27 to S29†). Stacks of N_a = 256 images were obtained at ψ = 30° for the (0–250) nm and (0–150) nm NDs, and at ψ = 60° for the (0–50) nm NDs. Analysis was carried out using the SE pairs. The resulting particle volume histograms using a ND refractive index[37] of n = 2.42 show a nearly exponential decay, and thus were fitted with an exponential distribution $p_0 \exp(-V_p/\overline{V})$, with the mean volume $\overline{V}$. NDs are typically brick shaped, hence we defined a characteristic particle size using a cube geometry as $S = \sqrt[3]{\overline{V}}$. Fig. 9 shows the volume distributions for each ND sample and the exponential fits. The mean volumes $\overline{V}$ were found to be 2.1 × 10^4 nm^3, 2.4 × 10^5 nm^3 and 4.1 × 10^5 nm^3, for the (0–50) nm, (0–150) nm and (0–250) nm NDs, respectively, yielding characteristic sizes S of 27.6 nm, 62.1 nm, and 74.3 nm.

3.8. Limitations and refinements

Let us review the assumptions of the method as presented, the resulting limitations, and further refinements possible.

(i) NPs are assumed to be smaller than the optical resolution of the microscope, in order to use the microscope PSF independent of the particle size in the analysis. This is relevant when using the SN pair and corresponding correction factors ρ, to minimize the noise in the retrieval of A_ϕ. For larger objects, one can use the C pair, and retrieve the integrated phase area similar to other quantitative phase imaging (QPI) techniques.[38] However, long-range phase gradients are difficult to determine with a DIC based approach, which measures only the spatial differential of the phase, while other QPI methods such as off-axis holography[38] are advantageous when used for measuring extended structured objects such as whole cells.

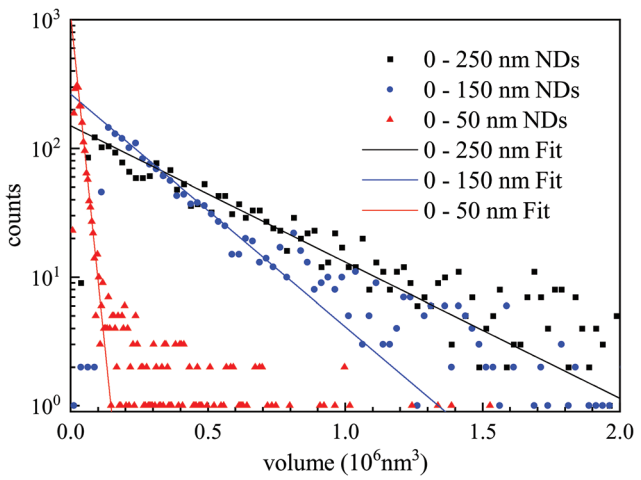

Fig. 9 Size histograms measured with qDIC on nanodiamonds in silicon oil. Particles with nominal diameter ranges (0–250) nm and (0–150) nm were measured using the 0.75 NA objective, while those with (0–50) nm diameters were imaged with the 1.27 NA objective. The SE pair was used for the analysis. Solid lines are the exponential fits.

(ii) The refractive index of the NPs is assumed to be constant over the probed wavelength range. Since the wavelength range has a relative bandwidth of only 10% and the NPs are assumed to be dielectric, this is not a limiting factor for the NPs investigated here. NPs showing a strong dispersion of the refractive index typically also show significant absorption, *e.g.* plasmonic NPs close to the plasmon resonances. They are less suited for the present method and can be better measured using their extinction cross-section.[8]

(iii) NPs are assumed to be non-birefringent. This is specifically relevant for the DIC method used in the present work, which is based on two sheared beams linearly polarized along and orthogonal to the shear. A birefringence aligned with the shear would thus be measured as a phase difference. Notably, such a signal, which is a single peak in δ, leads to a differential shape in the phase $\phi(\mathbf{r})$, which in first-order would not affect the integrated phase area A_ϕ. An instrumentation refinement suppressing this effect would be to add quarter wave plates on both sides of the sample to convert the orthogonal linear polarizations into circular polarizations of opposite helicity, probing the circular birefringence (optical activity), which is weak in natural materials. Notably, this would also suppress the triple pattern seen in the integrated phase for the high NA objectives (Fig. 1d) as a result of the elongated PSFs of linearly polarized light. However, a change of the polarization state of the transmitted light of the beams by a birefringence phase shift would still affect their recombination by the objective DIC prism, which would be relevant for strongly birefringent NPs.

(iv) NPs are assumed to have an isotropic response. An anisotropic response due to the NP shape would affect A_ϕ similar to the birefringence discussed in (iii). Elongated shapes result in a field-orientation dependent NP polarisability, which for smallelliptical NPs is given by the components[39]

$$\alpha_j = V\varepsilon_0 \frac{\varepsilon_{NP} - \varepsilon_m}{\varepsilon_m + L_j(\varepsilon_{NP} - \varepsilon_m)}, \qquad (21)$$

with the NP volume V, the relative permittivity of the NP ε_{NP} and the surrounding dielectric medium ε_m, the permittivity of free space ε_0, and the depolarisation factors L_j, for field polarizations along the three NP axes j = 1, 2, 3. We can see that for a small permittivity contrast $\eta = \varepsilon_{NP}/\varepsilon_m - 1$, we can develop $\alpha_j \approx V\varepsilon_0\eta(1 - L_j\eta) + O(\eta^3)$, showing that the orientation dependence is given by the factor $1 - L_j\eta$. The depolarization factors L_j are 1/3 for a sphere, and with increasing aspect ratio decrease towards zero along the long axis, and increase towards 1 along the short axis. Importantly, they are bounded between zero and one, so that for small η the anisotropy is small independent of shape, for NPs described by the dipole limit eqn (21). For typical organic particles in water, η is about 0.2, so that even for shapes with large aspect ratios the resulting differences between the α_j are below 10%.

For the ND samples investigated in the present work, the index contrast is higher, yielding $\eta \approx 1.5$, so that the effect can be more pronounced. The NDs have a range of brick-like shapes,[27] with aspect ratios of 1–1.5. In the data we find examples of the resulting asymmetric response in $\phi(\mathbf{r})$,

showing up as bipolar stripes tailing away from the ND, as is exemplified in the inset of Fig. S28.† Since the size distribution in the case of the NDs is wide, the resulting volume error is not important for the conclusions drawn.

(v) The permittivity contrast η is assumed to be small in order to neglect variations in beam propagation direction in the ray picture, or a significantly screened local field inside the particle in the wave-picture. Layered structures such as lipid bilayers[24] will be less affected by the screening due to the Maxwell's boundary conditions conserving the dominant in-plane field. For a higher index contrast, the above analytical expressions for elliptical particles could be a starting point to provide corrections.[6] For more complex shapes, full numerical simulations would be required to provide calibration-free quantitative sizing.[7] To avoid the complications of large $|\eta|$, one can choose a suited immersion medium, which is commercially available[40] with refractive indexes between 1.3 and 1.8.

(vi) Typical biological NPs such as endosomes, liposomes, or viruses, are not homogeneous in material and shape, so that the size and the composition cannot be easily separated. However, the phase area A_ϕ can still be used to determine the organic mass in the NP in a similar way as it is done in quantitative phase imaging of cells.[41] Combining this analysis with nanoparticle tracking to determine the NP hydrodynamic radius from the spatial diffusion would then allow to determine both size and mass of the particle.

Furthermore, for particles with unknown refractive index, a correlative measurement of the same particle in two different immersion media[7] can be used to determine the refractive index of each particle, analogous to the determination of the PS index using ensemble averaged phase areas in the ESI section S2†.

Finally, we note that apart from using calculated responses for sizing, there is the possibility to calibrate the method for a specific particle type by measuring particles of a range of known sizes.

4. Conclusion

In conclusion, we have investigated the application of quantitative DIC microscopy with Wiener filtering for sizing individual dielectric NPs, and determined the precision and accuracy of the method. Using polystyrene beads of 100 nm radius as size standard, we found that the accuracy in determining their radius was within few nm, corresponding to a relative accuracy of only a few percent. In terms of precision, we found the smallest detectable PS bead radius to be about 10 nm, limited by background structure at the glass interface onto which the nanoparticles were deposited. For reliable identification of NPs, a signal of at least four standard deviations above the background is required, corresponding to a radius of 16 nm. This has been verified experimentally using small fluorescent PS beads. Notably, this limit can be overcome when observing particles which attach and/or detach from a glass surface during measurements, eventually reaching a sensitivity only limited by shot noise. The latter was found to equate to 4 nm PS bead radius when averaging over 1000 frames, which can be achieved within 1 s total acquisition time with modern cameras. Such sensitivity could be further increased by using small phase offsets in the DIC acquisition, potentially reaching a size limit down to only 2 nm radius. As application example, we demonstrated sizing of individual nanodiamonds having poly-disperse distributions. Small nanodiamonds with nominal sizes below 50 nm were well above the detection limit, and were found to have a nearly exponential size distribution with 28 nm mean size.

Considering the importance of dielectric nanoparticles in many fields, from naturally occurring virions and exosomes to polluting nanoplastics, the proposed method could offer a powerful tool for nanoparticle analysis, combining accuracy, sensitivity and high-throughput with widely available and easy-to-use DIC microscopy.

Author contributions

W. L. and P. B. conceived the work. S. H. prepared the samples for the optical measurements and performed the related measurements and data analysis. D. R. and L. P. supported the data analysis. S. H., P. B. and W. L. wrote the manuscript. All authors contributed to the data interpretation and manuscript review.

CRediT: Conceptualization WL, PB; data curation SH, DR, LP, WL; formal analysis SH, WL, DR; funding acquisition WL, PB; investigation SH, DR; methodology WL, PB, SH, DR; project administration PB, WL; resources PB, WL; software WL, DR, LP; supervision WL, PB; validation SH; visualization SH, PB, WL; writing – original draft SH, WL, PB; writing – review & editing PB, WL, SH, DR, LP.

Data availability

Information on the data underpinning the results presented here, including how to access them, can be found in the Cardiff University data catalogue at http://doi.org/10.17035/d.2022.0153720825.

Conflicts of interest

There are no conflicts to declare.

Acknowledgements

S. H. acknowledges support for his PhD studies by the EPSRC Diamond Science and Technology CDT [grant no. EP/L015315/1] and Cardiff University. The microscope equipment was supported by the EPSRC grant no. EP/M028313/1. We acknowledge Joseph Bleddyn Williams for contributing to the development of the qDIC analysis software, Iestyn Pope for support of the

microscope instrumentation, Martina Recchia and Ozan Aksakal for measuring the bead fluorescence spectra, and Vikramdeep Singh for help with the atomic force microscopy measurements.

References

1 T. Sun, Y. S. Zhang, B. Pang, D. C. Hyun, M. Yang and Y. Xia, *Angew. Chem., Int. Ed.*, 2014, **53**, 12320–12364.
2 J. Liu, R. Zhang and Z. P. Xu, *Small*, 2019, **15**, 1900262.
3 Z.-M. Dang, J.-K. Yuan, S.-H. Yao and R.-J. Liao, *Adv. Mater.*, 2013, **25**, 6334–6365.
4 W. Anderson, D. Kozak, V. A. Coleman, Å. K. Jämting and M. Trau, *J. Colloid Interface Sci.*, 2013, **405**, 322–330.
5 S. Mourdikoudis, R. M. Pallares and N. T. K. Thanh, *Nanoscale*, 2018, **10**, 12871–12934.
6 L. M. Payne, W. Albrecht, W. Langbein and P. Borri, *Nanoscale*, 2020, **12**, 16215–16228.
7 Y. Wang, A. Zilli, Z. Sztranyovszky, W. Langbein and P. Borri, *Nanoscale Adv.*, 2020, **2**, 2485–2496.
8 L. M. Payne, W. Langbein and P. Borri, *Phys. Rev. Appl.*, 2018, **9**, 034006.
9 A. Zilli, W. Langbein and P. Borri, *ACS Photonics*, 2019, **6**, 2149–2160.
10 M. Piliarik and V. Sandoghdar, *Nat. Commun.*, 2014, **5**, 4495.
11 G. Young, N. Hundt, D. Cole, A. Fineberg, J. Andrecka, A. Tyler, A. Olerinyova, A. Ansari, E. G. Marklund, M. P. Collier, S. A. Chandler, O. Tkachenko, J. Allen, M. Crispin, N. Billington, Y. Takagi, J. R. Sellers, C. Eichmann, P. Selenko, L. Frey, R. Riek, M. R. Galpin, W. B. Struwe, J. L. P. Benesch and P. Kukura, *Science*, 2018, **360**, 423–427.
12 R. W. Taylor and V. Sandoghdar, *Nano Lett.*, 2019, **19**, 4827–4835.
13 C.-Y. Cheng, Y.-H. Liao and C.-L. Hsieh, *Nanoscale*, 2019, **11**, 568–577.
14 R. D. Boyd, S. K. Pichaimuthu and A. Cuenat, *Colloids Surf., A*, 2011, **387**, 35–42.
15 G. M. Nomarski, *J. Phys. Radium*, 1955, **16**, 9S.
16 M. R. Arnison, K. G. Larkin, C. J. R. Sheppard, N. I. Smith and C. J. Cogswell, *J. Microsc.*, 2004, **214**, 7–12.
17 S. V. King, A. Libertun, R. Piestun, C. J. Cogswell and C. Preza, *J. Biomed. Opt.*, 2008, **13**, 024020.
18 D. D. Duncan, D. G. Fischer, A. Dayton and S. A. Prahl, *J. Opt. Soc. Am. A*, 2011, **28**, 1297.
19 S. S. Kou and C. Sheppard, International Conference on Advanced Phase Measurements Methods in Optics and Imaging, 2010, pp. 301–306.
20 M. Shribak, K. G. Larkin and D. Biggs, *J. Biomed. Opt.*, 2017, **22**, 016006.
21 C. Ding, C. Li, F. Deng and G. J. Simpson, *Opt. Express*, 2019, **27**, 3837.
22 E. B. van Munster, L. J. van Vliet and J. A. Aten, *J. Microsc.*, 1997, **188**, 149–157.
23 K. Koos, J. Molnár, L. Kelemen, G. Tamás and P. Horvath, *Sci. Rep.*, 2016, **6**, 30420.
24 D. Regan, J. Williams, P. Borri and W. Langbein, *Langmuir*, 2019, **35**, 13805–13814.
25 D. Regan, J. Williams, F. Masia, P. Borri and W. Langbein, *Quantitative Phase Imaging V*, 2019.
26 C. I. McPhee, G. Zoriniants, W. Langbein and P. Borri, *Biophys. J.*, 2013, **105**, 1414–1420.
27 I. Pope, L. Payne, G. Zoriniants, E. Thomas, O. Williams, P. Watson, W. Langbein and P. Borri, *Nat. Nanotechnol.*, 2014, **9**, 940–946.
28 L. M. Payne, W. Langbein and P. Borri, *Appl. Phys. Lett.*, 2013, **102**, 131107.
29 L. Payne, G. Zoriniants, F. Masia, K. P. Arkill, P. Verkade, D. Rowles, W. Langbein and P. Borri, *Faraday Discuss.*, 2015, **184**, 305–320.
30 S. Inoué, *Exp. Cell Res.*, 1952, **3**, 199–208.
31 X. Xu, W. Huang and M. Xu, *Opt. Express*, 2015, **23**, 27911.
32 S. Inoué and W. L. Hyde, *J. Biophys. Biochem. Cytol.*, 1957, **3**, 831–838.
33 M. I. Shribak, S. Inoue and R. Oldenbourg, SPIE Proceedings, 2002.
34 P. Higdon, R. Juškaitis and T. Wilson, *J. Microsc.*, 1997, **187**, 8–11.
35 A. V. Kuhlmann, J. Houel, D. Brunner, A. Ludwig, D. Reuter, A. D. Wieck and R. J. Warburton, *Rev. Sci. Instrum.*, 2013, **84**, 073905.
36 M. Benelajla, E. Kammann, B. Urbaszek and K. Karrai, *Phys. Rev. X*, 2021, **11**, 021007.
37 G. Turri, S. Webster, Y. Chen, B. Wickham, A. Bennett and M. Bass, *Opt. Mater. Express*, 2017, **7**, 855–859.
38 Y. Park, C. Depeursinge and G. Popescu, *Nat. Photonics*, 2018, **12**, 578–589.
39 C. F. Bohren and D. R. Huffman, *Absorption and scattering of light by small particles*, John Wiley & Sons, New York, 1983.
40 https://www.cargille.com/refractive-index-liquids/.
41 T. A. Zangle and M. A. Teitell, *Nat. Methods*, 2014, **11**, 1221–1228.